Model-Based Performance Analysis of Pleated Filters with Non-Woven Layers

Eirini Velali[a,1], Jannik Dippel[b,1], Birgit Stute[a], Sebastian Handt[b], Thomas Loewe[b], Eric von Lieres[a,*]

[a]*Forschungszentrum Jülich GmbH, IBG-1:Biotechnology, Wilhelm-Johnen-Str. 1, 52425 Jülich, Germany*
[b]*Sartorius Stedim Biotech GmbH, August-Spindler-Str. 11, 37079 Göttingen, Germany*

Abstract

The water flow rates of commercial sterilizing grade 10" filter cartridges were simulated by Computational Fluid Dynamics (CFD) and compared to experimental data. This study compares four methods used to reconstruct the internal pleat geometry ranging from generic designs to analysis of microscopic images. The impact of the cartridges' plastic cage on flow resistance was studied and found to be negligible. A systematic overestimation of the simulated filter flow rate was attributed to additional hydrodynamic resistance of the non-woven material between the pleats. The permeability of the non-woven material was estimated by fitting CFD models to experimentally determined water flow rates and compared to the permeability of this material as directly measured with a flow cell. Good correlation between CFD-based estimations and directly measured values was found at low pressures, while differences at high pressures indicated the existence of further flow resistance, which is hypothesized to be caused by deformation of the pleat geometry under pressure.

Keywords: filter cartridge, membrane filter, non-woven layer, pleat reconstruction, computational fluid dynamics, flow resistance

1. Introduction

1.1. Pleated Filter Cartridges

Pleated filter cartridges for fluid filtration are widely used in a vast range of industrial applications, including waste water treatment, food and beverage, or water clarification for the microelectronic industry. The present study focuses on sterilizing filters used in pharmaceutical and biopharmaceutical processes ranging from cell culture media filtration to final fill applications. The products in this industry such as large protein therapeutic agents are highly sensitive to mechanical stress during the purification process (Aldington and Bonnerjea, 2007). Hence, a comprehensive understanding of the fluid dynamics in these filtration processes

*Corresponding author. Tel.:+49 2461 61 2168
Email addresses: e.velali@fz-juelich.de (Eirini Velali), jannik.dippel@sartorius-stedim.com (Jannik Dippel), b.stute@fz-juelich.de (Birgit Stute), sebastian.handt@sartorius-stedim.com (Sebastian Handt), thomas.loewe@sartorius-stedim.com (Thomas Loewe), e.von.lieres@fz-juelich.de (Eric von Lieres)
[1]These authors have contributed equally to this work.

is of particular interest. Nevertheless, the findings of this work can be transferred to filter cartridges in other industrial applications.

Fig. 1 shows a typical filter cartridge in which the pleated membrane is attached in the annular region between two concentric plastic cylinders with windows that serve as fluid inlets and outlets. The device contains two membrane layers, a pre-filter and a main filter that are pleated to increase the area per filter element. Located between the pleats are two non-woven layers to maintain a certain distance between the pleats and serve as drainage to ensure complete usage of the membrane area during filtration. Higher pleat density and more pleats enable a larger membrane area to be packed inside one filter cartridge. In particular, pleat height, pleat type and packing density can be varied.

Despite the importance in biopharmaceutical processes, little is known about the hydrodynamic flow in filter cartridges at operational conditions. Several research groups have shown that besides the permeability of the filter medium such as membrane, the pleating design of the filter cartridge can significantly impact the overall filter flow rate (Brown et al., 2009, 2010; Lutz, 2009). Dense pleating can decrease the flow rate in a filter cartridge by more than 50 % as compared with flat sheets of the same filter medium. Hence, the performance of industrial-scale pleated membrane cartridges, i.e. water flow rate at a given pressure, cannot easily be predicted from corresponding flat sheet data. However, previous studies are mostly empirical and lack a comprehensive analysis of several factors that impact on the fluid flow, such as pressure loss in the spacer material between the pleats or pleat shape deviations under operational pressure.

Overall, a better understanding of the fluid flow in pleated filter cartridges can help to predict shear stress in filter cartridges, and *in-silico* development can improve the design of pleated filter elements. Future *in-silico* development of filter cartridges can support faster optimization of filter geometry with regard to membrane, non-woven and pleating design as well as the plastic parts of the cage and the housing.

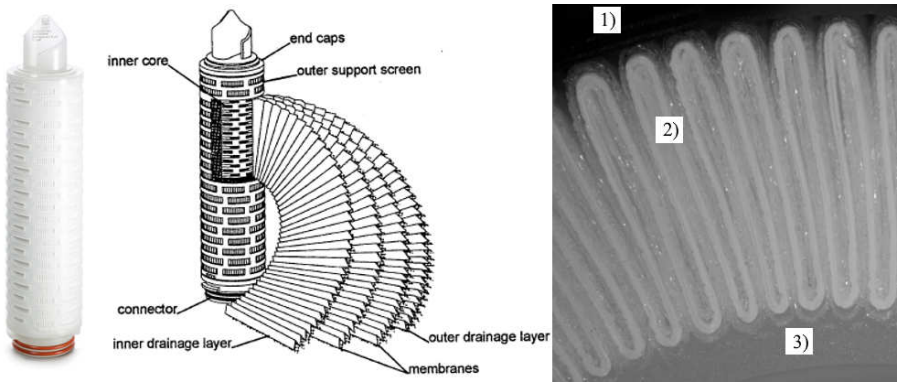

Figure 1: Filter cartridge. Full device with plastic cage *(left)*, schematic diagram *(middle)*, detail of cross section with pleated membrane *(right)*.

1.2. Model-Based Analysis

Several authors apply model-based methods for analyzing the performance of pleated cartridges in different application areas, including filtration of gases and liquids. Computational fluid dynamics (CFD) is commonly applied for analyzing hydrodynamics, using finite elements or finite volumes. However, previous studies are limited to simplified geometries. The models are mostly set up in two spatial dimensions and with generic pleat shapes. The latter implies the assumption that all pleats have precisely the same geometry and properties.

As illustrated in Fig. 1, there are three domains: 1) upstream of the membrane 2) the membrane 3) downstream of the membrane. The flow resistance of the layers of non-woven material is often neglected, as they have a much higher permeability than the membrane due to larger pores and a more open pore structure. However, these layers are key to maintaining the membrane in a specific shape, which is represented in the computational geometry.

Chen et al. (1995) study pleated filter panels with six commercial filter media for various air filtration applications. Their model describes one rectangular pleat in two spatial dimensions and is solved using the finite element method. The model is validated against experimental data from Yu and Goulding (1992). Depending on the pleat height, there is a specific pleat count that minimizes the pressure drop of the device. The model is applied to optimize the performance of rectangular pleated filters with varying geometry and filter media. In a similar study, Théron et al. (2017) evaluate the influence of pleat geometry on the pressure drop and air velocity field in coarsely pleated fibrous filters. They simulate half of one representative pleat in three configurations with different heights and widths. As expected, the pressure drop decreases as the pleat height diminishes and the pleat width increases. These results are validated against data obtained from experimental prototypes.

Chen et al. (2017) perform three dimensional simulations of single pleats in air filtration cartridges using the finite volume method. Four different pleat shapes are compared with respect to maximum and uniformity of the pressure field, which is important for reverse puls-jet cleaning. Subrenat et al. (2003) investigate a cylindrical pleated filter that is packed with activated carbon cloth for treating volatile organic compounds. They compare filters with 10, 30, 45 and 60 pleats. The computational domain describes one half pleat in three spatial dimensions and is also solved using the finite volume method. The model is applied to analyze the aerodynamic behavior in terms of pressure drop and flow structure. Additional criteria are homogeneity of the flow and utilization of the filter surface.

Gas filtration applications are often in the turbulent flow regime (Caesar and Schroth, 2002), whereas liquids are mostly incompressible and in the laminar flow regime. Hence, CFD simulations of gas filtration runs performed by several authors have limited transferability to liquid filtration trials. In the latter case, the regions upstream and downstream of the membrane are governed by Navier-Stokes equations, and Brinkman's

equation is used for describing media resistance in the porous region.

Wakeman et al. (2005) study laminar flow of an incompressible fluid in a filter cartridge similar to Fig. 1. Their model describes two pleats in two spatial dimensions and neglects the plastic parts of the housing. The model equations are solved using the finite element method. A separate model describes the effect of membrane compression and loss of filtration area due to geometric and hydrodynamic effects. When both models are combined, the simulated pressure drop of the cartridge matches experimental data. The percentage of effective filtration area was found to decrease with increasing pleat number due to pleat crowding and membrane compression, particularly towards the center of the device. On the other hand, increasing pleat height creates more space that can cause pleat deformation in the periphery of the device. Nassehi et al. (2005) study similarly shaped devices that are used for filtration of hydraulic fluids employed in aeronautical applications. They compare four different computational geometries with an increasing level of detail and two numerical solution schemes for the finite element method. The simulation results are validated against one another, but not compared with experimental data.

Other authors apply mathematical modeling for studying service life (Saleh et al., 2015) and fouling (Sanaei et al., 2016) of pleated filter cartridges, for example. However, these studies are related to intrinsic membrane properties rather than hydrodynamics between the pleats. Hydrodynamic flow patterns are also important for the performance of membrane adsorbers (Ghosh et al., 2013). They are usually studied under non-binding conditions. Understanding hydrodynamic effects in such devices is a key prerequisite for transferring membrane-related data across devices with different arrangements of the same membrane type. This particularly applies to scaling from small discs to large filter cartridges (Giglia et al., 2010).

1.3. Scope of this Study

The main objective of this work is to systematically analyze the performance of pleated filter cartridges for liquids using CFD simulations and to quantitatively compare the simulation results to experimental data. In particular, the study focused on the impact of important design characteristics, such as the outer support screen, the inner core and the drainage layers between the pleats on cartridge performance. Experimental data is obtained by measuring the flow rates of clean water in prototype cartridges such as shown in Fig. 1. The CFD simulations are solely based on the geometry of pleats and the housing and on material properties, i.e. permeability and porosity of membrane and non-woven layers. Here, the intrinsic permeability of the porous membrane is calculated from measured water flow rates of flat sheet membranes. Service life or fouling is not considered in this study.

Four different methods for reconstructing the pleat geometry in 2D cross-sections of the filter cartridges are implemented and compared to experimental data with regard to predicting water flow rates. Next, 3D simulations are applied to study the impact of the plastic cage on water flow rate.

For these simulations, the permeability of the non-woven layers that serve as drainage is assumed to be infinite. Differences observed between the CFD-simulated water flow rates and corresponding measurements are attributed to the hydrodynamic resistances of the non-woven. Hence, as a next step, the permeabilities of the non-woven material were directly measured using a flow cell. In addition, apparent permeabilities of the non-woven were estimated by fitting CFD simulations of the studied filter cartridges with finite non-woven permeability to the experimentally determined flow rates. These CFD estimated non-woven permeabilities were compared to the directly measured values.

2. Experimental setup

2.1. Water Flow Rate Measurements

Sterilizing grade 10″ filter cartridges with a pleat height of 11.5 *mm* were used. Prototype cartridges contained a heterogeneous double layer membrane, which is made of polyethersulfone and has a thickness of 160 μm for the pre-filter and 150 μm for the main filter. Four different prototype filters were built and measured in this study. One filter with 104 pleats (cartridge A) was used to compare different pleat reconstruction methods and to study the impact of the plastic cage. Three additional filters with 95 (cartridge B), 102 (cartridge B) and 110 (cartridge C) pleats were employed to study the influence of the pleat density.

Fig. 2 shows the experimental setup for water flow experiments. The cartridges were placed in a stainless steel housing and vented. The cartridges were first wetted for 300 *s* at a constant differential pressure of 0.3 *bar* between the inlet and outlet of the housing. Differential pressure was measured using two pressure sensors (Wika, $0-4$ *bar*). Subsequently, the water flow measurement was started. A pressure drop of 0.5 *bar* was applied to cartridge A. Pressure drops of 1.5, 1.0, 0.5, 0.3, 0.2 and 0.1 *bar* were applied to cartridges B, C and D. The differential pressure was controlled by a rotary pump (Koch, $0-4$ *bar*). The water flow rate was measured using a flow meter in the upstream piping next to the cartridge inlet. Each measurement was performed for 300 *s*. The temperature was controlled at $20 \pm 0.5\ ^{\circ}C$.

2.2. Membrane Permeability

In the CFD simulations, the membrane properties are defined by two parameters, porosity ε and intrinsic permeability k. The porosity is a fundamental membrane property, which is tightly controlled in the manufacturing process. The permeability has to be determined from experimental data. Typically, the water flow rate Q with the unit $\frac{m^3}{s}$ is measured using membrane samples with surface area A and thickness L at a defined pressure drop Δp. Flat disc membranes with an effective membrane area of 14.7 cm^2 were placed in a stainless steel housing. Before the flow was measured, the filters were wetted with water for 300 *s* at a pressure of 0.3 *bar*. The flow rate was then determined by gravimetry for 300 *s* at a pressure of 0.5 *bar*. Given the dynamic viscosity μ of the liquid, which is pure water in this study, Darcy's law permits to calculate the

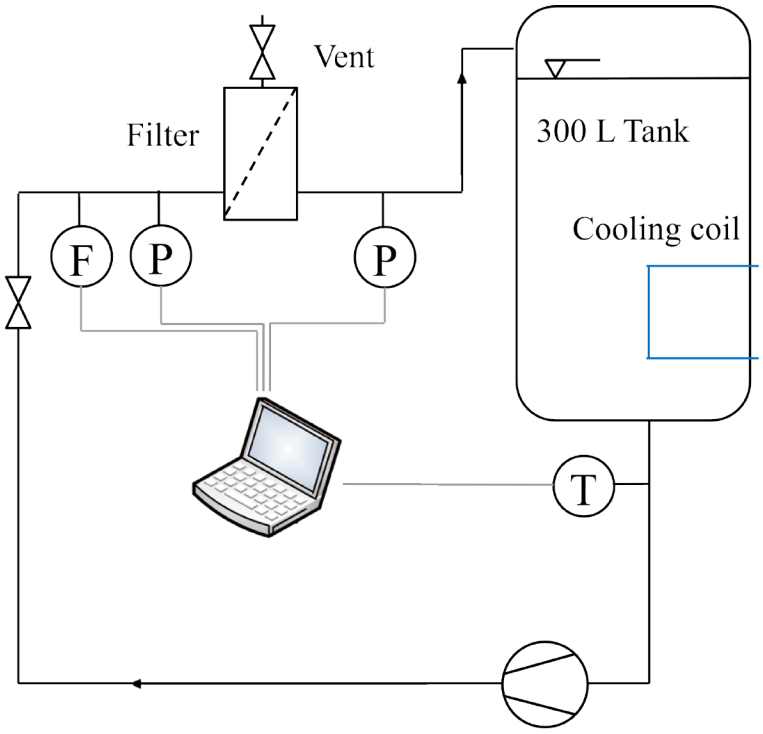

Figure 2: Schematic representation of the experimental setup to determine the water flow rate of 10" filter cartridges.

intrinsic permeability k with unit m^2, which is required by the CFD software, from the measured water flow rate (Hubbert, 1957):

$$Q = \frac{A\ k\ \Delta p}{\mu\ L} \tag{1}$$

Sterilizing grade filter devices, as shown in Fig. 1, often contain a heterogeneous double layer membrane. In case pre-filters are used, their porosity ε_i, permeability κ_i and thickness L_i can differ from the main filter. The geometry of the CFD simulations can be simplified by combining two membrane layers into one with a thickness L_{total} and permeability k_{total}. The total thickness is $L_{total} = L_1 + L_2$. The total permeability k_{total} can be calculated using Darcy's law, based on the equality of water flow rates normalized to the membrane area, $Q_{total} = Q_1 = Q_2$, and additivity of pressure drops, $\Delta p_{total} = \Delta p_1 + \Delta p_2$, in the membrane stack:

$$k_{total} = \frac{L_1 + L_2}{(\frac{L_1}{k_1} + \frac{L_2}{k_2})} \tag{2}$$

2.3. Non-Woven Permeability

Within the pleats of a filter cartridge, the fluid flows laterally through the non-woven in the drainage layer. To measure the lateral permeability of non-woven materials, a flow cell with an slit size was constructed (Fig.

3). A rectangular slit with an adjustable height h_{slit} between 400 and 800 μm is positioned between two parallel poly(methyl methacrylate) plates. The inlet of the flow cell is connected to a pressurized vessel filled with water. Two pressure indicators (Wika, $0 - 4$ bar) are placed at positions P_1 and P_2 (Fig. 3). The differential pressure between them is adjustable. The path length l between the two pressure sensors is 0.15 m. The width w of the slit is 0.125 m. The borders are sealed with silicone.

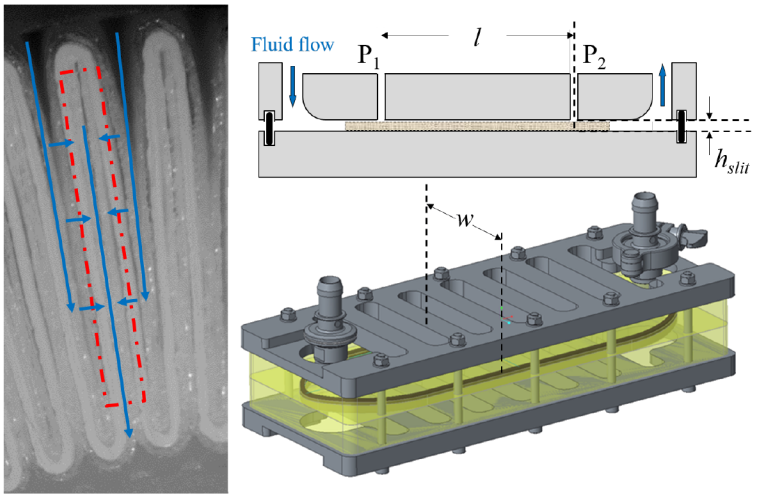

Figure 3: Schematic representation of the experimental setup to simulate the flow through a pleat in a filter cartridge. Fluid flows laterally through the non-woven in a pleat and passes through the membrane in a direct flow path *(blue arrow on the left image)*. The fluid flow through the non-woven is simulated in a flow cell setup. A schematic 3D image *(top)* and a cross section *(bottom)* are shown on the right side. The fluid flows in the directions indicated by the blue arrows. The non-wovens are placed in the red framed area, and the pressure difference is measured between two pressure sensors P_1 and P_2

Rectangular samples of the non-woven material were placed in the flow cell (right hand side of Fig. 3) so that the flow was directly laterally. The plates are stabilized by a stainless steel frame to avoid any deformation during pressurization and measurements. Samples of the non-woven were prepared as 0.125 x 0.2 m^2 sheets in two, three and four layers. The thickness of each sample was measured before the sample was inserted into the measurement area of the flow cell. The thickness was measured at a pressure of 5 Pa using the universal micrometer F16.50200 (Frank-PTI GmbH) with an measuring accuracy of 1 μm. The slit height was varied to study the influence of compression of the non-woven material on its hydrodynamic resistance.

The water flow rates at differential pressures of 0.2, 0.5, 0.4 and 1.0 bar were calculated from gravimetry data for a measurement time of 120 s using a Quintix 5102-1S balance (Sartorius) at a temperature of 20 ± 0.5 $°C$. Each experiment was performed in triplicate with different non-woven samples. Based on the measured flow rate data, the permeabilities k of the non-woven samples were determined according to Eq. (1). The mean and standard deviation of these permeabilities were individually determined for each set of non-woven layers.

3. Pleat Geometry Reconstruction

Precise reconstruction of the pleat geometry is crucial for quantitative prediction of filter cartridge performance. The right hand side of Fig. 1 shows an example microscopic image of a filter cross section with star pleat geometry. Four different approaches were developed and compared in this study (Fig. 4). For reconstruction of the pleat geometry, variations along the height coordinate of the cartridge were neglected, and a two-dimensional cross section was considered to be representative of the whole cartridge.

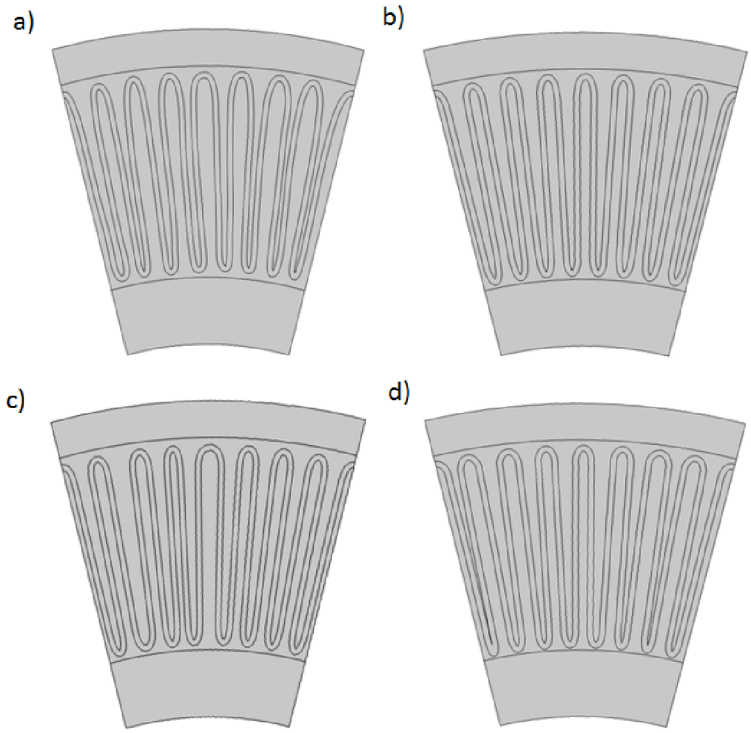

Figure 4: Pleat geometry as reconstructed by a) image analysis, b) regular generic design, c) deterministic irregular design, and d) randomized irregular design.

3.1. Image Analysis Design

In this approach, the curvature of the membrane, which is folded into pleats, is reproduced manually by Bézier curves. This reproduction is based on microscopic images using Inkscape. The computational geometry is completed by adding two concentric circles that describe the inlet and the outlet boundaries (Fig. 5, left). The resulting geometry is imported into the CFD software COMSOL Multiphysics 5.2a. The membrane is defined as porous region, whereas the remaining space is defined as a free region for all simulations, where the non-woven is neglected. Alternatively, several membrane and/ or non-woven layers with different thicknesses and material properties can be created around the center line.

The microscopic image provides information on a cross section of the whole device, but in many cases only a sector is shown (Fig. 1). In the latter case, side boundaries of this sector need to be added to the computational geometry. In order to represent the whole capsule, periodic boundary conditions are applied at both sides of the sector. To do so, the ends of the reconstructed membrane region have to be manually adjusted such as to match each other's positions. Boundary conditions are defined at the inlet and outlet as well as at the sides in case only a sector is provided.

3.2. Regular Generic Design

In this approach, the center line of the membrane is described by a simple mathematical function, Eq. (3), assuming that all pleats are identical. This function depends on the number of the pleats, N_p, a form factor, p, and on the radial extension of the pleated region between r_2 and r_3. The radii r_1 and r_4 will later be used to confine the computational domain (Fig. 5, left). The function is defined in four steps (Fig. 5, right): First, a periodic curve $h(\phi)$ with the specified number of pleats is created in the Cartesian coordinate system using the sine function, Eq. (3a). Then, the shape of the pleats is adjusted using the form factor, p, according to Eq. (3b). In the Cartesian coordinate system, increasing the form factor makes the pleat edges more parallel and the outer and inner caps more spherical (Fig. 5, right). In other words, the form factor determines the width of the turn of the pleated membrane. Third, the resulting function is stretched and shifted according to the radial position, Eq. (3c). Finally, the created membrane curvature is transformed from Cartesian coordinates into radial coordinates using the standard transformation rules for the resulting x and y positions as given in Eq. (3d). Bézier points are calculated in MATLAB, using Eq. (3a) to Eq. (3d) and imported to the Inkscape vector graphics editor. In Inkscape, the same procedure as for the image analysis design is then followed.

$$h_1 = sin(\phi N_p) \quad \text{with} \quad \phi \in [0, 2\pi] \tag{3a}$$

$$h_2 = sign(h_1) * abs(h_1)^{1/p} \tag{3b}$$

$$h_3 = r_2 + (r_3 - r_2) * (1 + h_2)/2 \tag{3c}$$

$$x = h_3 * sin(\phi) \quad \text{and} \quad y = h_3 * cos(\phi) \tag{3d}$$

3.3. Deterministic Irregular Design

This approach combines features of image analysis and generic designs. The membrane path is not followed in full detail, but the microscopic image is used only for measuring the width of each pleat. A generic design is created with the same number of pleats, which are then individually stretched or compressed in order to match the measured widths. This procedure is implemented in MATLAB before the Bézier points

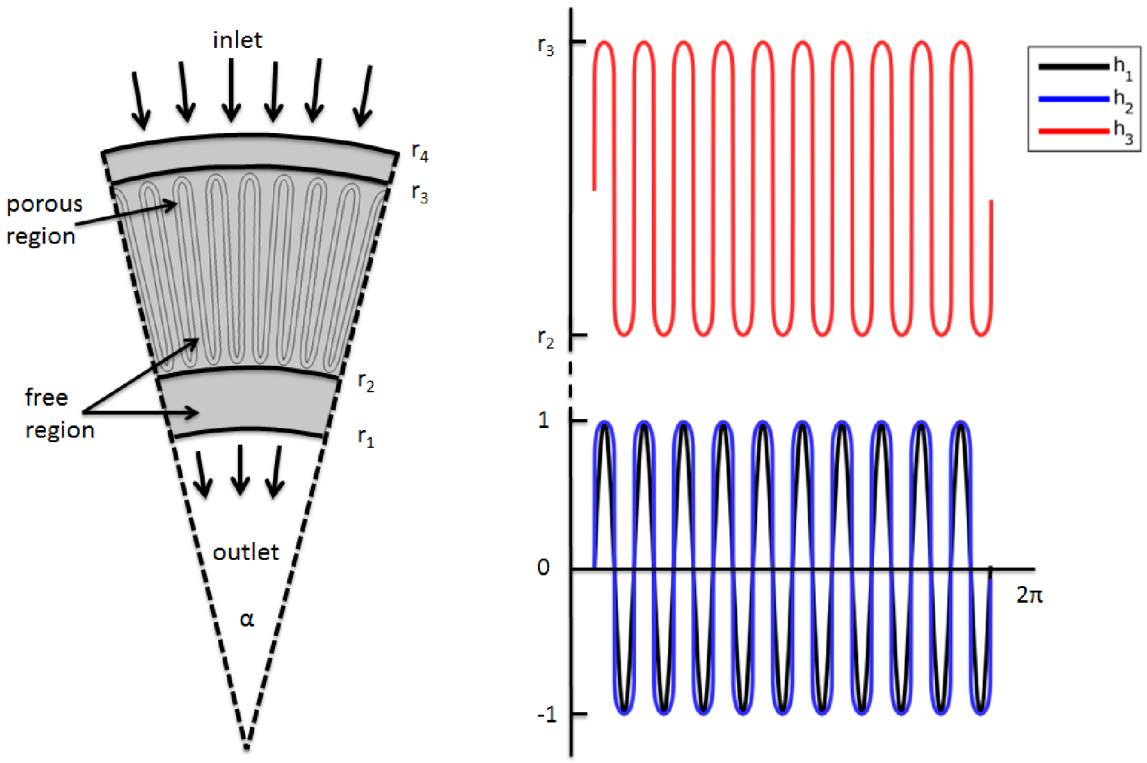

Figure 5: Sketch of computational geometry (2D cross section, left) and stepwise procedure for generic reconstruction of membrane curvature using Eq. (3) (right). See online version of this article for line colors.

are imported to Inkscape. As in the image analysis design, the reconstructed geometry is often limited to a sector of the cross section that is covered by the microscopic image.

3.4. Randomized Irregular Design

As in the deterministic irregular design, this approach is also based on a generic design, which is then modified by adjusting the width of each individual pleat. However, the measured widths are not directly used, but their statistical distribution is first analyzed and then random numbers are generated following this distribution. This statistical analysis not only considers the mean and variance of all measured pleat widths but also correlations between the width of neighboring pleats. Randomized designs have the advantage that full cross sections can be reproduced even if only a sector is covered by the analyzed image. Moreover, several reconstructions of the same device can be created with different random numbers for analyzing the impact of such natural variations.

4. Plastic Cage Geometry

As shown in Fig. 1, the pleated membrane is supported by a cage. Two plastic cylinders, the outer support screen and the inner core, contain openings through which the liquid can pass. These channels are

arranged in rings of staggered rectangular windows. Fig. 6 illustrates the size and position of these windows. The outer windows cover 45.1 % of their boundary to the inlet channel and 27.7 % of their boundary to the pleated membrane region (r_3 in Fig. 5, left). The inner windows cover 9.2 % of their boundary to the outlet channel and 25.1 % of their boundary to the pleated membrane region (r_2 in Fig. 5, left). In the CFD simulations, the part between r_2 and r_3 in Fig. 5 (left) is extruded to the third dimension and placed between the plastic parts, as illustrated in Fig. 6. Symmetry allows to reduce the computational complexity of 3D simulations by considering only one ring. The computational geometry is created based on imported Computer-Aided Design (CAD) data from the plastic manufacturing. In combination with the cage, a full 2D cross section of the pleated membrane geometry needs to be reconstructed. This cross section is placed in the center and extruded to the third dimension in order to match the height of the plastic ring (Fig. 6). A representative flow pattern is created by applying inlet and outlet boundary conditions at the upstream end of the peripheral channel and at the downstream end of the central channel, respectively, and wall boundary conditions elsewhere.

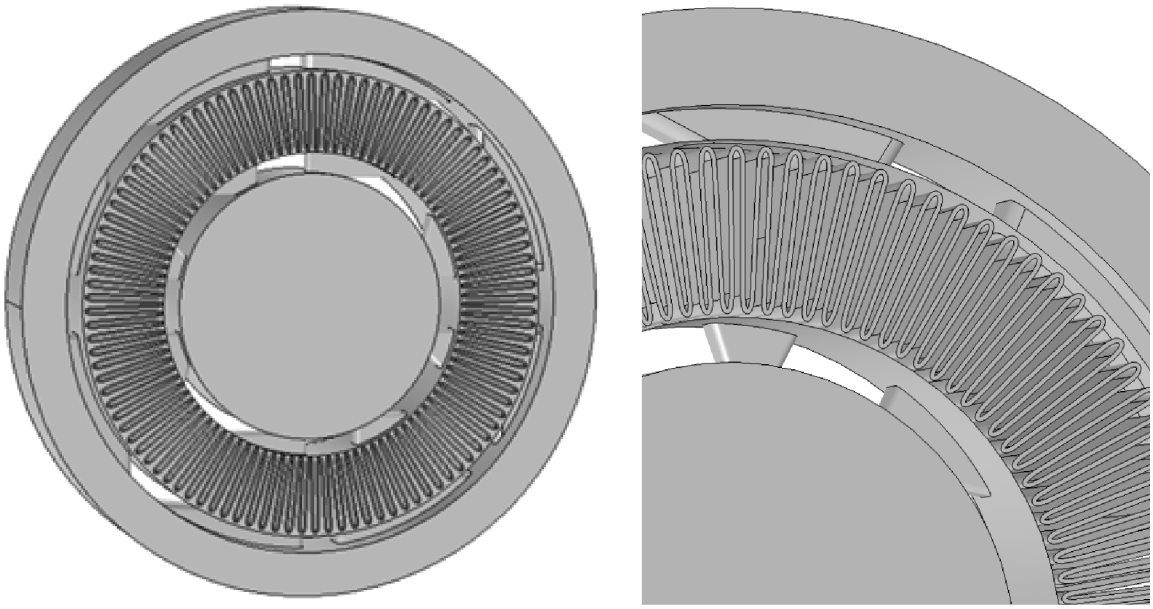

Figure 6: Computational geometry with plastic cage (3D ring, left). Detail magnification with transparent void between pleated membrane layers (right).

5. Computational Fluid Dynamics

CFD simulations are based on fundamental conservation laws of mass, momentum and energy (Lomax et al., 2003). These laws are expressed by partial differential equations whose boundary conditions are defined by the computational geometry. In the presented study, water flow can be assumed to be laminar and

incompressible. The free regions, which are situated between the membrane pleats and at the inlet and outlet, Fig. 5 (left), are described by Navier-Stokes equations:

$$\rho(\frac{\partial \upsilon}{\partial t} + \upsilon\nabla\upsilon) = -\nabla p + \nabla(\mu(\nabla\upsilon + (\nabla\upsilon)^T) \tag{4a}$$

$$\nabla\upsilon = 0 \tag{4b}$$

In Eq. (4), ρ is the density, υ the velocity and p the local pressure of the liquid. The membrane region, as a porous domain, is described by Brinkman's equation:

$$\rho(\frac{\partial \upsilon^*}{\partial t} + \upsilon^*\nabla\upsilon^*) = -\nabla p + \nabla(\mu(\nabla\upsilon^* + (\nabla\upsilon^*)^T) - \frac{\mu}{k}\upsilon^* \tag{5a}$$

$$\nabla\upsilon^* = 0 \tag{5b}$$

In Eq. (5), $\upsilon^* = \frac{\upsilon}{\varepsilon}$ is the interstitial velocity.

Stationary solutions of eqs. (4)-(5) are computed in COMSOL Multiphysics 5.2a for specific pressure drops across the outer boundaries of the imported geometry. For the 2D simulations, the outer boundaries are given by the arcs at r_1 and r_4 in Fig. 5 (left). Periodic boundaries are implemented by identifying the dashed lines at both sides of the grey area in Fig. 5 (left). For the 3D simulations, the inlet is defined at the front side of the outer ring in Fig. 6 and the outlet at the back side of the central disc. Vanishing normal flow is used as boundary conditions at all other outward faces in Fig. 6. No slip boundary conditions are applied at the inner and outer surfaces of the membrane layer, i.e. the tangential component of surface velocity between the void and porous regions is zero. This is justified by the fact that the largest pressure drop in the system occurs across the membrane layer, and consequently the liquid flow is practically orthogonal to both sides of the membrane. For the same reason, the intrinsic permeability, k, is assumed to be isotropic. The computational domain is meshed using unstructured triangular elements, and the direct MUMPS solver is used. All simulations are performed on several meshes with increasing element numbers until the resulting flow rates varied by less than 1 %. Tab. 1 provides an overview of the geometric parameters of the filter cartridges used for the CFD simulations.

6. Results and Discussion

6.1. Comparison of Pleat Reconstruction Methods

Fig. 7 shows the results of 2D simulations using the four pleat geometry reconstruction methods at a pressure drop of 0.5 *bar*. As expected, the flow rate strongly increases in the gaps between the membrane pleats. Due to the constant thickness and homogeneous material properties of the membrane layer(s) and

Table 1: Geometric parameter of CFD simulated filter cartridges.

Parameter	Value	Unit
Membrane thickness	313	μm
Non-woven thickness	260 (B, C, D)	μm
Membrane permeability	$1.03 \cdot 10^{-14}$	m^2
Membrane porosity	79	%
Non-woven porosity	79 (B, C, D)	%
Pleat height	11.5	mm
Inner boundary (r_1)	44	mm
Outer boundary (r_4)	71	mm
Pleat number	104 (A), 95 (B), 102 (C), 110 (D)	–

because the largest part of the pressure drop occurs across these layer(s), the flow rate is very uniform within the membrane region. It is also rather uniform in the inlet channel, but jets occur in the outlet channel that are caused by the membrane pleats. With all four pleat reconstruction methods, the periodicity at the side walls of the simulated sector is clearly visible. Only in the regular generic design, Fig. 7b, are all pleats identical, while various differences can be observed in the other panels of this figure. The image analysis design, Fig. 7a, is most elaborate in following every detail of the membrane curvature. Only the width of each pleat is precisely reproduced in the irregular generic design, Fig. 7c, while the random generic design, Fig. 7d, features the same pleat width distribution.

The simulated flow velocity profiles resulting from the four different pleat reconstruction methods, as compared in Fig. 7, exhibit some distinct qualitative differences of the local flow velocities in the pleats. Unfortunately, the local flow rates cannot be directly compared to measurement data, as such experiments cannot be performed with sufficient precision. However, the simulated water flow rates can be extrapolated from the simulated cross section for the entire cartridge in order to calculate the total water flow rate of the 10” cartridge. This allows direct comparison with measurement data. The results for 0.5 *bar* are shown in Fig. 8.

Deviations between the predicted and the measured flow rates are between 9.71 – 16.25 %, depending on the pleat reconstruction method. Theses differences are mainly caused by the differing flow field between the pleats. The flow field in the channels upstream and downstream of the membrane has very little influence on the resulting water flow rates, as the pressure drop across these regions is very little (Fig. 9). In all 2D simulations, the predicted flow rates are systematically larger than the measured ones. This can be attributed to the fact that several flow resistances were neglected in the simulations. Subsequently, these potential additional flow resistances are analyzed in more detail. The flow rates simulated using the image analysis

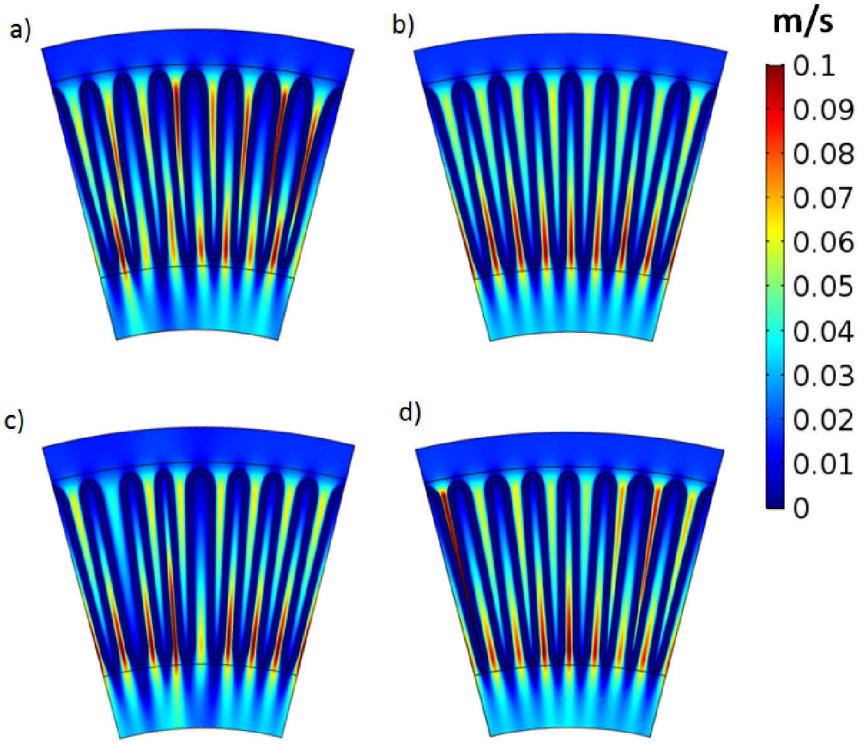

Figure 7: Simulated velocity profiles in a 2D cross section for a pressure drop of 0.5 *bar* and pleat geometry reconstructed by a) image analysis, b) regular generic design, c) irregular generic design, and d) randomized generic design.

and irregular generic designs match the measured data more closely than those simulated using the regular generic and randomized generic designs, since the pleat geometry is reproduced in more detail. Overall, a more detailed reconstruction of the pleat design results in a more accurate flow rate prediction. Hence,

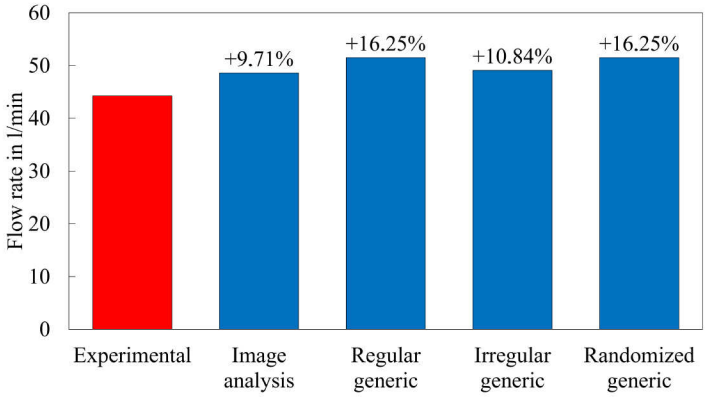

Figure 8: Water flow rates as measured and simulated in 2D with extrapolation to the whole cartridge at 0.5 *bar*. Deviation between simulation and measurement are shown in percent.

the local flow profile is supposed to be more accurate as well. However, the pleat reconstruction by image analysis is more labor-intensive than it is for generic designs.

6.2. *Impact of Plastic Cage*

Further simulations are performed to analyze the difference between simulated and measured flow rates. These simulations explicitly account for the flow resistance caused by the plastic cage. Hence, they need to be performed in 3D and require the membrane pleating to be reconstructed for a full 2D cross section of the cartridge. The regular generic design is used in the 3D simulations, which are computationally much more expensive. The simulated velocity profiles with and without considering the plastic cage as well as the simulated pressure profiles are shown in Fig. 9 for a pressure drop of 0.5 *bar*. The simulated flow rate of the 2D simulations is 51.5 $\frac{L}{min}$, whereas the flow rate of the 3D simulation without the plastic cage is 51.8 $\frac{L}{min}$ and that with the plastic cage is 50.5 $\frac{L}{min}$.

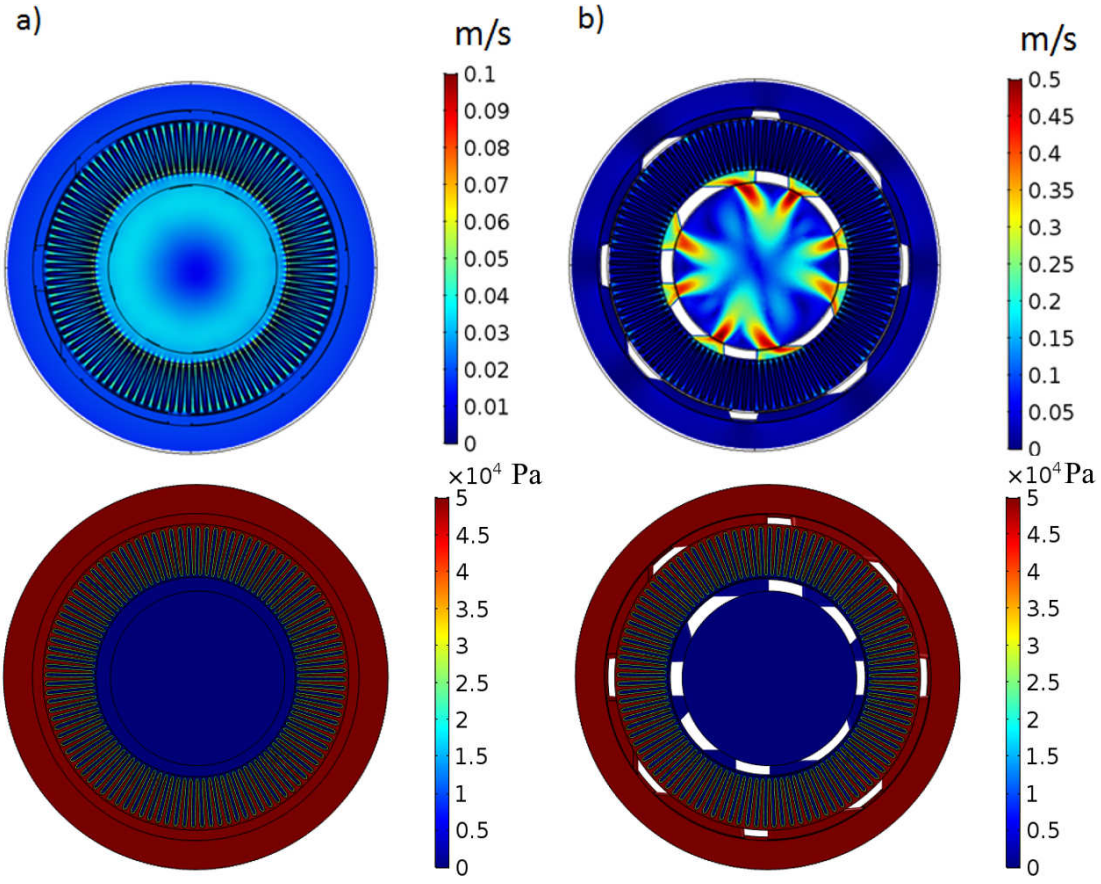

Figure 9: Simulated velocity profiles (top) and pressure profiles (bottom) in a 3D ring for a pressure drop of 0.5 *bar* and pleat geometry reconstructed by regular generic design. For comparison with 2D simulations, plastic parts are modeled as a) permeable and b) impermeable. Both panels show a central cross section through the simulated ring.

Comparison between 2D and 3D simulations without the plastic cage allow quantification of the numerical approximation error of the CFD simulations in this case study. For all three pressure drops studied, the impact of the plastic cage on the flow rate is in the same order as the numerical approximation error. In conclusion, the flow resistance caused by the plastic parts can be neglected, independently of the pleat reconstruction method. Furthermore, the pressure drop in the inlet region upstream of the membrane pleats as well as in the core is negligible compared with the pressure drop across the pleated membrane region. The remaining difference between simulations and measurements, which is between 9.7 % and 16.3 % at a pressure drop of 0.5 *bar*, is presumably caused by the omitted hydrodynamic resistances due to the non-woven layers between the membrane layers.

6.3. Impact of Non-Woven Material

Three prototypes (cartridges B, C and D) are used to analyze the impact of the non-woven material in the drainage layer on the water flow rate. These cartridges have similar material properties to those of cartridge A. Since high quality microscopic images of the full cross section are available for these prototypes, the image analysis design was used for reconstructing the geometry. Fig. 10 depicts the experimentally determined water flow rates of the three cartridges as well as the predicted water flow rate with the assumption of infinite non-woven permeability. In the CFD simulations, infinite permeability is implemented by replacing the respective porous region by a void region. As for cartridge A (104 pleats, shown above), the predictions for cartridge B (95 pleats) and cartridge C (102 pleats) at 0.5 *bar* deviate from the corresponding water flow rate measurements by less than 10 %. However, the predictions for cartridge D with a higher pleat density (115 pleat) deviate more strongly (17.4%) from the corresponding measurements. At an increased pressure drop of 2.0 *bar*, the simulations overpredict the measured water flow rates even more by up to 33 % for cartridges B and C and up to 44 % for cartridge D. In other words, the simulation error increases as do the pleat density and pressure.

The non-woven permeabilities of cartridges B, C and D are estimated by fitting CFD simulations to experimentally measured water flow rates at different pressure drops. The results in Tab. 2 to Tab. 4 indicate that the non-woven material is more permeable than the double layer membrane with a permeability of $1.03 \cdot 10^{-14}$ m^2 by about four orders of magnitude. Nevertheless, it has a significant influence on the flow of water through the filter cartridge. This can be attributed to the fact that membrane is crossed by the bulk flow in an axial direction while flow passes through the majority of non-woven layers in a lateral direction.. Consequently, the length of the flow path through the membrane, which is the membrane thickness, is shorter by two magnitudes than through non-woven material, which can be as long as the pleat height. Conversely, the cross-sectional area of the membrane that is effectively exposed to the water flow is larger by two orders of magnitudes than the area of the non-woven layers.

The CFD estimated non-woven permeabilities depend on the pressure drop even though the permeability

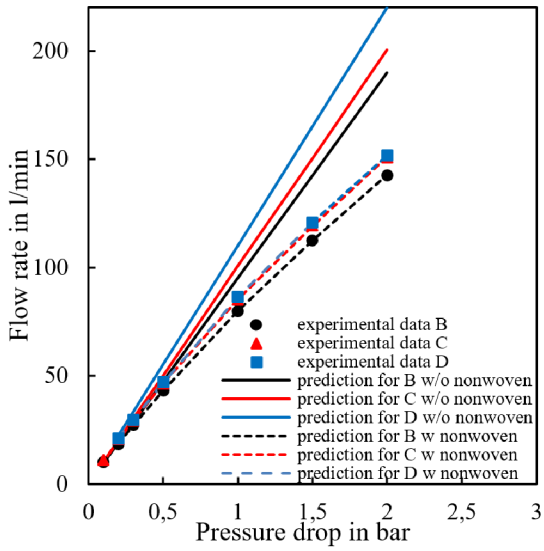

Figure 10: Experimental and simulated water flow rates of cartridges B, C and D with infinite and estimated permeabilities of the non-woven material.

Table 2: Water flow rates of cartridge B as measured and simulated in 2D with and without non-woven layer, and CFD estimated non-woven permeabilities. The difference between measured and simulated values is shown in parentheses.

Pressure drop bar	Experimental water flow rate $\frac{L}{min}$	2D Simulated water flow rate without non-woven layers $\frac{L}{min}$	CFD estimated non-woven permeability k m^2
0.1	10.1	9.5 (-5.9 %)	–
0.2	18.5	19.1 (+3.2 %)	$2.26\ 10^{-10}$
0.3	27.3	28.6 (+4.8 %)	$1.60\ 10^{-10}$
0.5	43.3	47.6 (+9.9 %)	$0.73\ 10^{-10}$
1.0	79.8	95.1 (+19.2 %)	$0.36\ 10^{-10}$
1.5	112.5	142.7 (+26.8 %)	$0.25\ 10^{-10}$
2.0	142.7	190.0 (+33.1 %)	$0.19\ 10^{-10}$

is strictly a material property. Moreover, some simplifications are made: 1) the non-woven material is considered to be isotropic, and 2) the compression of the non-woven towards the center of the filter is not taken into account. Hence, the estimated non-woven permeabilities are apparent values that do not represent true material properties.

The intrinsic permeability of the membrane layers was derived from water flow rate measurements, yet direct measurements of the permeability of the non-woven layer are more complicated. The non-woven material is generally anisotropic, i.e., the permeability can vary substantially between axial and lateral flow

Table 3: Water flow rates of cartridge C as measured and simulated in 2D with and without non-woven layer, and CFD estimated non-woven permeabilities. The difference between measured and simulated values is shown in parentheses.

Pressure drop bar	Experimental water flow rate $\frac{L}{min}$	2D Simulated water flow rate without non-woven layers $\frac{L}{min}$	CFD estimated non-woven permeability k m^2
0.1	11.2	10.1 (-9.8 %)	–
0.2	20.7	20.2 (-2.4 %)	–
0.3	29.4	30.3 (+3.1 %)	$3.80\ 10^{-10}$
0.5	46.5	50.4 (+8.4 %)	$1.27\ 10^{-10}$
1.0	85.1	100.6 (+18.2 %)	$0.55\ 10^{-10}$
1.5	119.3	150.6 (+26.2 %)	$0.37\ 10^{-10}$
2.0	150.9	201.6 (+33.6 %)	$0.28\ 10^{-10}$

Table 4: Water flow rates of cartridge D as measured and simulated in 2D with and without non-woven layer, and CFD estimated non-woven permeabilities. The difference between measured and simulated values is shown in parentheses.

Pressure drop bar	Experimental water flow rate $\frac{L}{min}$	2D Simulated water flow rate without non-woven layers $\frac{L}{min}$	CFD estimated non-woven permeability k m^2
0.1	11.4	11.1 (-2.6 %)	–
0.2	21.2	22.2 (+4.7 %)	$2.97\ 10^{-10}$
0.3	29.8	33.3 (+11.7 %)	$1.15\ 10^{-10}$
0.5	47.1	55.3 (+17.4 %)	$0.75\ 10^{-10}$
1.0	86.3	110.1 (+27.6 %)	$0.45\ 10^{-10}$
1.5	120.9	164.6 (+36.1 %)	$0.34\ 10^{-10}$
2.0	151.7	218.8 (+44.2 %)	$0.27\ 10^{-10}$

directions. As described in the experimental section, a flow cell was constructed to measure the non-woven permeability in a lateral flow direction. The flow cell has a slit with a defined height h_{slit} in which the non-woven material can be compressed. Two, three and four layers of non-woven were measured at various differential pressures. Here, the compression factor c is determined by the height of the slit h_{slit} and the thickness of the non-woven sample $h_{non-woven}$.

$$c = \frac{h_{non-woven} - h_{slit}}{h_{non-woven}} \tag{6}$$

Fig. 11 compares the permeability of the non-woven material as measured using the flow cell with many

different layers and estimated by fitting CFD simulations to measured water flow rates through the entire filter cartridge. As expected, the non-woven permeability measured using the flow cell is independent of the number of layers used. At very low pressures (0.2 *bar*), the estimated permeabilities of cartridge B and D match the measured value within the standard deviation. However, the CFD estimated permeability of cartridge C is higher by 35 % than the measured value. Here, the estimated non-woven permeabilities decrease as the pressure increases. As previously discussed, the permeability is a material property and should hence be independent of the pressure, as is the case for the flow cell measurements. However, a slight decrease in the measured permeability can be observed when the compression factor is increased from 0.0 to 0.4. This is accompanied by a decreasing porosity of the non-woven material upon compression. Nonetheless, the permeability of the compressed non-woven material measured in the flow cell is by far not reduced sufficient to quantitatively explain the additional flow resistance that is observed across the cartridges at high pressure drops. Therefore, it can be hypothesized that the pleats in the cartridge are deformed at higher pressure, and hence the pleat reconstruction does not represent the actual geometry during operation of these filter cartridges. This will be thoroughly analyzed in a forthcoming study.

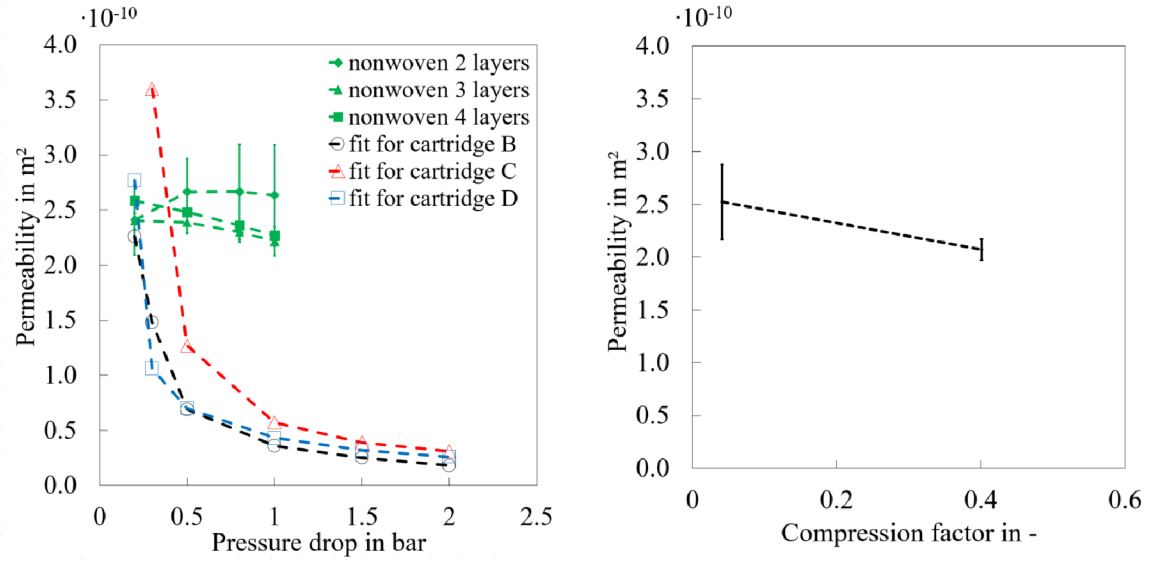

(a) Non-woven permeability estimated by CFD simulations of cartridges B, C and D versus permeability measured in the flow cell with 2, 3 and 4 non-woven layers (n=3).

(b) Experimentally determined permeability of the non-woven layers by the use of flow cell measurements for different non-woven compression factors (n=3).

Figure 11: Estimated and measured non-woven permeabilities. Lines are added to provide visual guidance.

7. Conclusions and Outlook

In the presented study, model-based analysis of different pleated filter cartridges was performed. Four different reconstruction methods for membrane pleats in a commercial 10" filter cartridge were compared with respect to their ability to predict the measured water flow rate at 0.5 *bar*. The pleat reconstruction methods are based on a microscopic image of a 2D cross section of the cartridge. In comparison of the simulated water flow rates to experimental values, the best results were obtained for the image analysis approach with an overestimation of about 10 %. In this approach, the membrane curvature is followed in full detail, which is laborious and potentially restricted to a sector of the cross section that is covered by the microscopic image. However, similar results can be achieved by adjusting the pleat width of a simple generic design such that the width of each pleat is exactly reproduced without considering further variations among the pleat shapes. Using this approach, the calculated water flow rates overpredict the experimental values by approx. 16 %. For all four reconstruction approaches, the CFD simulations systematically overpredict the experimental flow rates. Using 3D simulations of the filter cartridge, the impact of the plastic cage on the water flow rate was assessed. These simulations are computationally much more expensive. However, the results show that the plastic cage does not significantly contribute to the overall flow resistance of the analyzed cartridge at the pressure drops studied, indicating that the major hydrodynamic resistance is within the membrane and the membrane pleating.

Subsequently, three cartridge prototypes with varying pleat densities were constructed and analyzed at different pressures. At higher pressures, the overestimation of the simulated flow rate increased by about 30 % at 2 *bar*. These deviations are attributed to the omission of non-woven layers in the cartridge, even though these are highly porous. In further CFD simulations, the non-woven was considered, and its permeability was estimated such that the simulated water flow rates match the corresponding experimental data. These values were compared to the non-woven permeability as determined experimentally by a tailor-made flow cell. At pressures below 0.5 *bar*, the CFD estimated non-woven permeability closely matches the directly measured one. However, the CFD estimated non-woven permeability decreases significantly as pressure increases. The non-woven permeability as a material property cannot depend on the pressure drop, as is observed for the directly measured values.

Consequently, there must be an additional resistance that increases with pressure and is not considered in the CFD simulations. This is likely caused by the fact that the pleat geometry is assumed to be static, i.e., independent of the applied pressure. Yet during filtration, potential shifts in the pleat geometry can influence the fluid flow through the cartridge. Moreover, changes in pleat geometry might decrease the permeability of the non-woven by compression. Geometry changes during operation of such filter cartridges have not been studied yet, since methods to investigate such effects under process conditions are challenging. Further investigations are needed in order to obtain more accurate CFD predictions of the internal fluid flow.

The significance of the non-woven layer for the performance of pleated filter cartridges has not been recognized so far in the scientific community, and in particular, the contribution of the three major mass transfer resistances could not be quantitatively distinguished. These findings provide crucial information to further improve the design of such cartridges both in academia and in the industry. The models provided in this study can help to further analyze and efficiently design these cartridges, thus save costs and time-consuming experiments. In summary, the flow rate of unused cartridge can be predicted with high accuracy. This development will pave the way for analyzing other retention mechanisms, including effects such as pore blockage and cake formation.

8. Acknowledgements

The authors gratefully acknowledge financial support provided by the German Federal Ministry of Education and Research (BMBF), grant no. 13N13117.

9. References

Aldington, S. and Bonnerjea, J. (2007). Scale-up of monoclonal antibody purification processes. *Journal of chromatography*, 848:6478.

Brown, A., Levison, P., Titchener-Hooker, N., and Lye, G. (2009). Membrane pleating effects in 0.2 μm rated microfiltration cartridges. *Journal of Membrane Science*, 341(1):76–83.

Brown, A., Titchener-Hooker, N., and Lye, G. (2010). Scale-down prediction of industrial scale pleated membrane cartridge performance. *Biotechnology and bioengineering*, 108(4):830–838.

Caesar, T. and Schroth, T. (2002). The influence of pleat geometry on the pressure drop in deep-pleated cassette filters. *Filtration & Separation*, 9:48–54.

Chen, D.-R., Pui, D. Y. H., and Liu, B. Y. H. (1995). Optimization of pleated filter designs using a finite-element numerical model. *Aerosol Science and Technology*, 23(4):579–590.

Chen, S., Wang, Q., and Chen, D.-R. (2017). Effect of pleat shape on reverse pulsed-jet cleaning of filter cartridges. *Powder Technology*, 305:1 – 11.

Ghosh, P., Vahedipour, K., Lin, M., Vogel, J. H., Haynes, C., and von Lieres, E. (2013). Computational fluid dynamic simulation of axial and radial flow membrane chromatography: Mechanisms of non-ideality and validation of the zonal rate model. *Journal of Chromatography A*, 1305:114 – 122.

Giglia, S., Rautio, K., Kazan, G., Backes, K., Blanchard, M., and Caulmare, J. (2010). Improving the accuracy of scaling from discs to cartridges for dead end microfiltration of biological fluids. *Journal of Membrane Science*, 365(1):347–355.

Hubbert, M. K. (1957). Darcy's law and the field equations of the flow of underground fluids. *International Association of Scientific Hydrology. Bulletin*, 2(1):23–59.

Lomax, H., Pulliam, T., and Zingg, D. (2003). *Fundamentals of Computational Fluid Dynamics*. Scientific Computation. Springer Berlin Heidelberg.

Lutz, H. (2009). Rationally defined safety factors for filter sizing. *Journal of Membrane Science*, 341:268278.

Nassehi, V., Hanspal, N., Waghode, A., Ruziwa, W., and Wakeman, R. (2005). Finite-element modelling of combined free/porous flow regimes: simulation of flow through pleated cartridge filters. *Chemical Engineering Science*, 60(4):995 – 1006.

Saleh, A., Tafreshi, H. V., and Pourdeyhimi, B. (2015). Service life of circular pleated filters vs. that of their flat counterpart. *Separation and Purification Technology*, 156:881–888.

Sanaei, P., Richardson, G. W., Witelski, T., and Cummings, L. J. (2016). Flow and fouling in a pleated membrane filter. *Journal of Fluid Mechanics*, 795:3659.

Subrenat, A., Bellettre, J., and Cloirec, P. L. (2003). 3-d numerical simulations of flows in a cylindrical pleated filter packed with activated carbon cloth. *Chemical Engineering Science*, 58(22):4965 – 4973.

Théron, F., Joubert, A., and Le Coq, L. (2017). Numerical and experimental investigations of the influence of the pleat geometry on the pressure drop and velocity field of a pleated fibrous filter. *Separation and Purification Technology*, 182:69–77.

Wakeman, R., Hanspal, N., Waghode, A., and Nassehi, V. (2005). Analysis of pleat crowding and medium compression in pleated cartridge filters. *Chemical Engineering Research and Design*, 83(10):1246 – 1255.

Yu, H. H. and Goulding, C. H. (1992). Optimized ultra high efficiency filter for high-efficiency industrial combustion turbines. *atmosphere*, 1:1.